Microfluidic Synthesis of Hydrogel Microparticles with Superparamagnetic Colloids Embedded at Prescribed Positions for Anticounterfeiting Applications

Zhang, Mengmeng; Warth, T.; Boon, Niels; Demirörs, Ahmet Faik; Eral, Hüseyin Burak

DOI
10.1002/admi.202200899

Publication date
2022

Document Version
Final published version

Published in
Advanced Materials Interfaces

Citation (APA)
Zhang, M., Warth, T., Boon, N., Demirörs, A. F., & Eral, H. B. (2022). Microfluidic Synthesis of Hydrogel Microparticles with Superparamagnetic Colloids Embedded at Prescribed Positions for Anticounterfeiting Applications. *Advanced Materials Interfaces*, *9*(29), Article 2200899. https://doi.org/10.1002/admi.202200899

ADVANCED MATERIALS INTERFACES
www.advmatinterfaces.de

Microfluidic Synthesis of Hydrogel Microparticles with Superparamagnetic Colloids Embedded at Prescribed Positions for Anticounterfeiting Applications

*Mengmeng Zhang, Thom Warth, Niels Boon, Ahmet Faik Demirörs, and Hüseyin Burak Eral**

A microfluidic platform for continuous synthesis of hydrogel microparticles with superparamagnetic colloids (SPCs) embedded at prescribed positions is described. The shape of the cross-linked microparticle is independently controlled by stop–flow lithography, whereas the position of trapped SPCs are dictated by virtual magnetic moulds made of 2D nickel patches facilitating magnetic trapping. The spatial positions of trapped SPCs collectively function as a binary code matrix for product authentication. Analytical and finite element methods are combined to optimize the trapping efficiency of SPCs by systematically investigating magnetic field microgradients produced by nickel patches. It is envisioned that the proposed magnetic microparticles will contribute to the development of soft matter inspired product quality control, tracking and anti-counterfeiting technologies.

1. Introduction

Globalization has enabled unprecedented ease of access to products for consumers. However, this ease of access has also exposed consumers to an alarming number of counterfeit products.[1,2] This is especially worrisome when the products targeted are vaccines, antibiotics, and other life-saving commodities. While the products themselves are difficult to imitate, labels and packaging can be easily manipulated. Common counterfeiting strategies include: i) tampering with the details on authentic packaging (e.g., altering the expiry date), ii) using authentic packaging for counterfeit products to pass off counterfeits as authentic. In response, manufacturers and researchers have developed advanced packaging solutions. Some representative solutions are barcodes, holograms, sealing tapes, radio frequency identification devices,[3] watermarks, and optical/chemical/biological (DNA) tags.[4] Unfortunately, most of these solutions are not widely implemented due to their high cost and complicated authentication schemes.

As a potentially powerful tool to combat rampant counterfeiting on the packagings, the on-dose authentication (ODA) measure used as "in-drug labelling" is introduced.[5] ODA enables verification of the end product as genuine and ODA labels are usually made from biocompatible or edible materials that are directly embedded into the end products themselves. Bio-based materials are a promising class of materials that are currently under explored for ODA applications.[6–9] ODA technologies include Quick Response (QR) microtaggants,[10] encoded-multifunctional hydrogel microparticles,[7,11–13] physically unclonable function (PUF) barcodes,[14] 3D printed medicines[15,16] and safety-oriented photolithography of edible pharmaceutical polymer films.[17] Compared to traditional authentication protocols, ODA labels are more robust and resilient. ODA labels themselves cannot be easily tampered with without damaging the integrity of the product and fabrication of ODA labels requires highly specialized equipment and skilled operators, both of which are not easily accessible to counterfeit syndicates. Scalable production of ODA labels is possible through micro-scale fabrication techniques based on microfluidics[7,12,13] and customizable codes embedded in ODA labels such as QR microtaggants[10] and encoded-multifunctional hydrogel microparticles[7] can be easily read using current smartphone technology. ODA labels can also be 3D printed at centimeter-scale[15] for easy authentication by naked eyes.

Despite these advantages, ODA labels are not widely implemented yet due to difficulty in striking a balance between ease of verifying the authenticity and cryptographic safety. To illustrate this point, let's take the example of PUF barcode.[14] The PUF barcodes provide very high cryptographic safety yet accessing the stored information is not straightforward. Only a cryptographic key can read these ODAs under a series of light illumination with various excitation wavelengths. Consequently, the information in PUFs described by Leem et al.[14] can only be authenticated with dedicated lab equipment not available readily to end users. The need for dedicated lab equipment

---

M. Zhang, T. Warth, N. Boon, H. B. Eral
Process & Energy Department
Delft University of Technology
Leeghwaterstraat 39, Delft 2628 CB, The Netherlands
E-mail: h.b.eral@tudelft.nl

A. F. Demirörs
Complex Materials
Department of Materials
ETH Zürich
Zurich 8093, Switzerland

The ORCID identification number(s) for the author(s) of this article can be found under https://doi.org/10.1002/admi.202200899.

DOI: 10.1002/admi.202200899

increases the cost of PUF ODA limiting their utilization in low-cost products. On the other end of the spectrum, ODA measures produced by flow lithography[7] utilize the shape of the barcode to store information and cell-phones can be used for authenticity verification. In other words, they are easier to produce and authenticate yet they do not provide the high level of cryptographic safety PUFs provide. Ideal ODA should not be only easy to read but also it should provide high level of cryptographic safety. In this sense, a dual-authentication ODA label utilizing both optical and magnetic verification is a step in the right direction.

In this study, magnetic ODA labels made of hydrogel microparticles with superparamagnetic colloids embedded at prescribed positions were synthesized using a microfluidic approach. This approach parleys stop–flow lithography (SFL)[18] with virtual magnetic moulds (VMMs)[19] made of magnetically activated nickel patches. The pattern of Ni patches collectively denotes a binary code. The embedding efficiency was optimized through a combination of analytical scaling arguments and finite element simulations. The resulting hydrogel microparticles can effectively function as magnetic ODA labels with dual-authentication (optical and magnetic) providing additional cryptographic security than the previously proposed hydrogel microparticles[7] offering only optical authentication.

2. Results and Discussion

2.1. Hydrogel Microparticle Synthesis Strategy

The four steps to synthesize hydrogel microparticles are depicted in **Figure 1**a,b. First, a suspension containing UV-responsive oligomer (PEGDA), a photoinitiator, and SPCs are pumped into the channel (illustrated in Figure 1b as “Fill” step). SPCs are initially scattered randomly due to Brownian motion (Figure S1, Supporting Information). After the channel is filled, flow is stopped and an external magnetic field is imposed using a ring-shaped permanent magnet. SPCs move toward the Ni patches and are

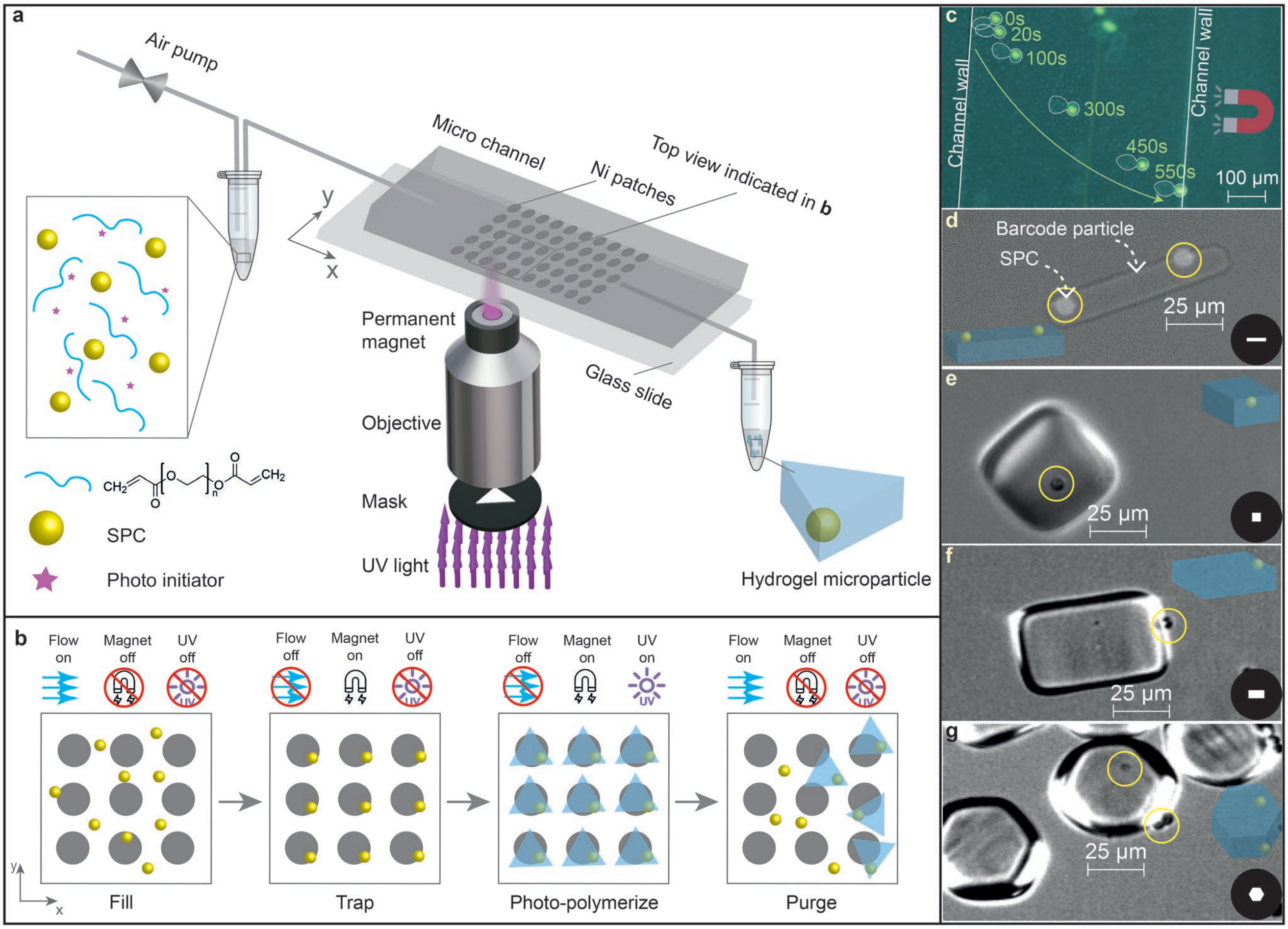

Figure 1. Scheme of the hydrogel microparticles synthesis. a) Solution containing polymer (PEGDA), photoinitiator and superparamagnetic colloids(SPCs) are pumped through a microfluidic channel. The VMMs placed on the bottom of the channel are magnetized on-demand to trap SPCs. UV light passing through a mask placed at the field stop of the microscope crosslinks the PEGDA to trap SPCs are designated positions. b) Illustration of four steps involved in synthesis from the top view. c) Hydrogel microparticles responds to the external magnetic field and moves from one channel wall to the other when a permanent magnet is brought in contact. Extracted from Movie S1 (Supporting Information). d–g) The microscopy pictures of microparticles of different shapes with SPCs placed at designated position. Their scale bars are all 25 µm. The mask used in synthesis of each particle is given along with a 3D illustration of the microparticle with embedded SPC.

assembled into a pattern dictated by the VMMs as shown in Figure 1b as “Trap” step. Next, a beam of UV light is passed through a mask to trigger photo-polymerization in the geometry dictated by the mask in “Photo-polymerize” step. After synthesis is completed, the channel is purged and the microparticles are collected in “Purge” step. The microparticles can be synthesized in batch mode by keeping the suspension in the channel stagnant while the microscope objective is moved along the channel using an automated stage[7,20] or they can be synthesized in continuous mode commonly referred to as stop–flow lithography.[18,21] When the continuous mode is desired, the suspension continuously flows into the channel via a pressure-regulated air pump while the synthesis of microparticles is realized through a series of photo-polymerization and magnetic trapping steps repeated. The canonical process flow is outlined in Figure 1b: Step I. Fill: pressure on, magnet off, shutter closed –1 s; Step II. Trap: pressure off, magnet on, shutter closed –1 s; Step III. Photo-polymerize: pressure off, magnet on, shutter on –0.5 s. Step IV. Purge: pressure on, magnet off, shutter closed –1 s.

The shape of the microparticle is controlled by the mask used during photo-polymerization, while the pattern of the SPCs is dictated by the lithographically deposited pattern of the VMMs. Microparticles of various shapes with SPCs embedded at designated positions were produced (strips, squares, rectangles, and hexagons) and are presented in Figure 1d–g. The top and bottom insets show the 3D illustration of the microparticle with embedded SPCs and the mask, respectively. We note that SPCs were successfully embedded regardless of microparticle shapes and were responsive to an external magnetic field (see Figure 1c and corresponding Movie S1, Supporting Information). We envision that response of synthesized microparticles toward an external field illustrated in Figure 1c may be utilized to first collect microparticles dispersed in a liquid formulation and then to check the for the authenticity by decoding the binary code. Moreover, the existence of magnetic response as illustrated in Figure 1c may be interpreted as the first step of a dual-authentication process followed by optical authentication as illustrated by Rehor et al.[7]

The incorporation of VMMs[19] in SFL technology[22] affords several advantages. First, magnetic assembly of materials is contactless that is highly desirable in the manufacture of edible ODA labels and particles.[6,9,11,23,24] Second, the fidelity of assembling materials using magnetic moulds is shown to be as high as 97%[19] that is promising for applications requiring high encoding accuracy and capacity. Third, the production of nickel patches acting as VMMs requires highly precise techniques such as electron beam deposition that is not easily accessible and hence serves as a technological barrier to counterfeiting operations. Fourth, precise and highly customizable ODA labels[25–30] can be mass-produced via SFL.[18,31] Leveraging both optical and magnetic authentication schemes, a higher level of cryptographic safety can be achieved in a single scheme.[7]

Other methods such as 3D printing,[32] micro-engraving,[5,33] and 2-photon lithography[34] have also been considered from resolution and regulatory compliance point of view for synthesis of proposed microparticles. 3D printing has seen considerable interest in literature as certain drug excipients in molten form or as a viscous formulation can be extruded, providing easy route to commercialization with minimal regulatory hindrance. However, for most of the 3D printer types, the feature resolution depends highly on the designed geometry and print orientation and usually >10 µm. The same resolution issue is also relevant in micro-engraving. 2-Photon lithography offers nanometer resolution yet this comes at the expense of very slow operation. Beyond resolution issues, all these methods are not continuous, forcing us to choose stop–flow lithography as the ideal manufacturing method for this study.

Since the magnetic microparticles are proposed for labeling pharmaceuticals, the biosafety and cytotoxicity of the ingredients are essential to evaluate. Poly-ethylene glycol (PEG) is commonly used as an excipient in pharmaceutical formulations, and it is approved for clinical use by Food and Drug Administration due to its acceptable biosafety.[35] Iron oxide nanoparticles are found to be biocompatible and stable in aqueous solutions. Due to this nature, iron oxide nanoparticles have been employed for multiple clinical applications.[36] The trace of polystyrene in the SPC is deemed acceptable if the daily intake is <1.5 mg.[12] The only biosafety concern is the fluorescent dye adopted in the SPC. However, the fluorescent dye is utilized for visualization purposes in this study and can be removed in real-life applications since the barcode decoding can perform visable light microscopy. Therefore, we generally consider the proposed magnetic microparticles biosafe. Moreover, the photo-polymerized PEG hydrogels are also considered biosafe that have been widely used in cell encapsulation[37] and tissue engineering fields.[38] Therefore, it is possible to find many equivalent hydrogel materials[7,30,39,40] for the purpose of this work when the cytotoxicity of PEGDA is considered of ultimate importance in some application fields.

In addition to the cytotoxicity, another concern for the real-world application is the deformation of PEG hydrogel microparticles upon exposure to high humidity conditions. Due to its hygroscopic nature, microparticles may swell and deform anisotropically resulting in deformation of the code. Thankfully, the swelling ratio of PEG hydrogels can be adjusted by cross-link density via manipulating the monomer molecular weight, initiator concentration, irradiation time, and light intensity.[41,42] Moreover, the PEG hydrogels coding can be made in a way that after homogeneous swelling the code reads the same. Here, we will not explore this large parameter space in this study. However, it is should be noted that durability of the microparticles should be optimized to minimize deformations in proposed microparticles taking into account the exact storage conditions of the product. Furthermore, superparamagnetic iron oxide nanoparticles are widely applied for electromagnetic interference shielding;[43,44] therefore, there is a concern that our composite particles might have decreased durability due to the electromagnetic Interference pollution. However, our binary code only is exposed to magnetic field produced by a permenant magnet when authenticated. The dose and duration of exposure are relatively trivial. Therefore in this study, the durability of binary code in the presence of electromagnetic interference pollution is not further explored.

2.2. Optimization of Trapping Efficiency

Despite its promise, there are two major issues with the proposed microparticle manufacturing process. The first issue is the long time duration required to trap for SPCs on VMMs (referred to as trapping time). Our experiments showed that trapping time could be as long as a few minutes (Movie S4, Supporting Information) that is far from our desire of a few seconds. The second issue is authentication failure due to the incorrect placement of SPCs on VMMs. SPCs have to be trapped in the specific configuration outlined by the magnetic moulds, so that the binary code can be decoded successfully. However, as depicted in Figure 3a, some SPCs (highlighted in red) are deposited in the voids between Ni patches or no SPCs are trapped on some patches (highlighted in blue). A simple solution to address the issue with SPCs sedimenting in the voids might be to decrease the distance between VMMs. Yet this solution is not practical as the photolithography step is less reliable when distances less than one micron. One may also rationalize that increasing the concentration of SPCs will result in fewer unoccupied VMMs yet high volume fractions might cause aggregation/chaining of SPCs under the magnetic force and further exacerbate reading failure due to SPCs sedimenting at voids. At the same time, to ensure the edibility of this ODA code, we limit the selection of raw materials to the generally recognized as safe list. For instance, magnetic susceptibility tuning agents commonly used in magnetic trapping[19] are intentionally avoided due to their toxicity. To address these issues, a better understanding of the forces acting on the colloids in the presence of magnetic field gradients induced by VMMs is crucial. Therefore, we explored two scenarios as represented in **Figure 2**a and **Figure 3**b and will discuss them in the following sections.

2.2.1. Force Balance in Scenario A: Optimizing the Magnetic Microgradient Along z for Trapping Time

As schematized in Figure 2a, Scenario A assumes a SPC is sedimenting from a certain height above the Ni patch center through a liquid. As a results, it will experience magnetic force ($\vec{F_m}$), hydrodynamic drag force ($\vec{F_d}$), buoyancy ($\vec{F_b}$), and gravitational force ($\vec{F_g}$).

We first investigate the magnetic force, which depends on the Ni patch and SPC size, in combination with the position of SPC relative to patch. Specifically, we look at the vertical (z) component of this force along z-axis in our calculation of the trapping time. Using the magnetic force as in,[19] we find that its vertical component $F_{m,z}$ is given by

$$F_{m,z} = 4\pi r^3 \mu_0 \frac{\chi_{part} - \chi_{sol}}{\chi_{part} + 2\chi_{sol} + 3} |\vec{H}| \frac{\partial|\vec{H}|}{\partial(z)} \tag{1}$$

in which r is the radius of the SPC, μ_0 is the magnetic permeability of free space, χ_{part} and χ_{sol} are the magnetic susceptibility of SPC and the solution. Here, μ_0, χ_{part}, and χ_{sol} are constant. The microgradient $|\vec{H}|\frac{\partial|\vec{H}|}{\partial z}$ is directly proportional to the magnitude of the magnetic force, which depends on the magnetic field strength $H = |\vec{H}|$ and its gradient along the vertical (z) axis.

We use the COMSOL Multiphysics package as a finite element analysis tool to calculate the vertical magnetic force $F_{m,z}$ acting on a SPC placed at a canonical height of 10 µm above a single circular Ni patch for a various combinations of D_{SPC} and D_{patch}, as shown in Figure 2b. The depicted range of D_{SPC} and D_{patch} is chosen to represent the relevant experimental values in this study. The canonical height of 10 µm is chosen as the channel height is 35 µm and SPC sizes range from 1.43 to 10.3 µm (described in Experimental Section). As seen in Figure 2b, the colloid will experience a stronger magnetic force if it sediments onto a larger D_{patch}. This is further demonstrated in Figure S3 (Supporting Information): a larger Ni patch is able to produce a stronger microgradient, hence a larger magnetic force. Similarly, the size of D_{SPC} also exhibits a positive correlation because a larger volume SPC interacts stronger with the magnetic field in comparison to a smaller one.

Using $F_{m,z}$ calculated for various D_{SPC} and D_{patch} values, we can compare the magnitude of all possible forces acting on the SPC in Scenario A and identify the dominating force for the SPC sedimentation. The magnitude of all the other forces, i.e., the hydrodynamic drag force (F_d), buoyancy (F_b), gravitational force (F_g), and apparent Brownian force (F_r), are represented by

$$\begin{aligned} F_b &= \rho_l g \frac{4\pi}{3} r^3 \\ F_d &= 6\pi \nu \mu r \\ F_g &= \rho_p g \frac{4\pi}{3} r^3 \\ F_r &= \zeta m_p \sqrt{\frac{216 k_b}{\pi \left(\frac{\rho_p}{\rho_l}\right)^2 C_{Cun}}} \sqrt{\frac{\eta_f T}{\rho_l d^5 \Delta t}} \end{aligned} \tag{2}$$

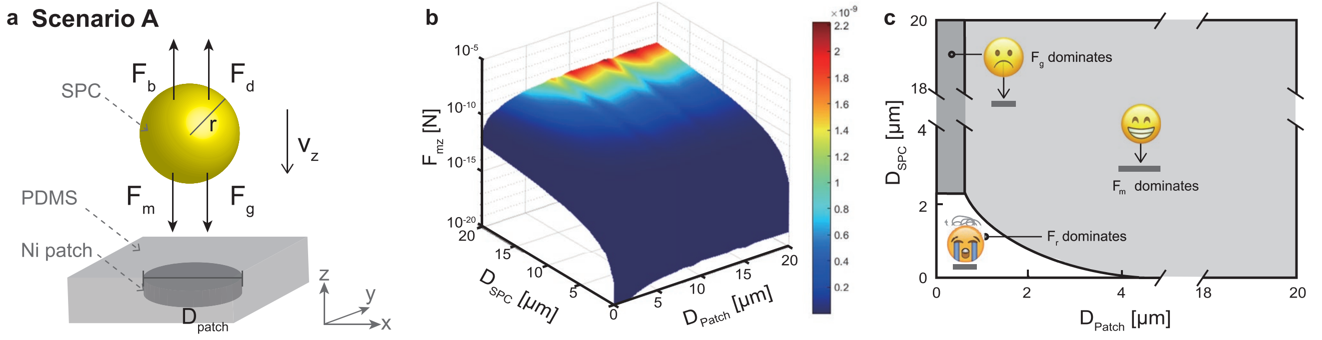

Figure 2. Analysis of forces acting on SPC based on Scenario A. a) Scenario A: SPC sedimenting above a Ni patch and the forces acting on the SPC are illustrated. b) The magnetostatic force, $F_{m,z}$ exerted on the SPC due to magnetic field gradient created by the Ni patch, obtained through Equation (1). c) The phase map of the dominating force.

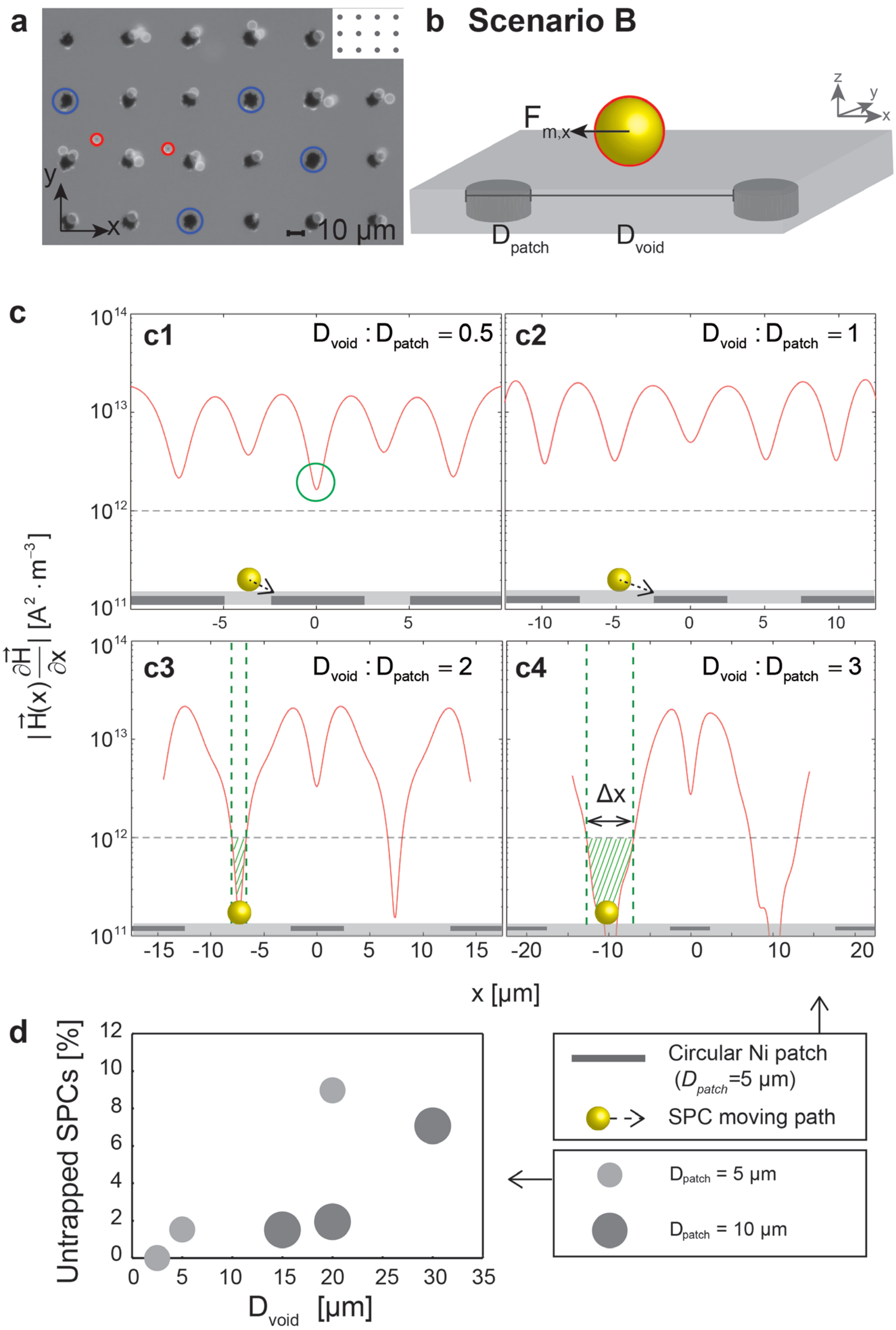

Figure 3. a) Micrograph illustrating the challenges in defining optimal experimental parameters for high fidelity trapping of SPCs . SPCs (10 vol.%, $D_{\{SPC\}}$ = 4.54 µm) are trapped by circular Ni patches (D_{patch} = 10 µm,D_{void} = 30 µm) in the presence of an external magnetic field. The insert shows the pattern of the Ni patches used. Two failure events are highlighted (i) SPCs that can be not trapped by Ni patches highlighted by red circles and (ii) empty patches where no SPC is trapped highlighted in blue. b) Scenario B: SPC settles between Ni patches. c) The horizontal microgradients $|\vec{H}|\frac{\partial \vec{H}}{\partial x}$ induced by Ni patch array of various voids as a function of position. The diameter of the patches D_{patch} is 5 µm while the distance of two adjacent Ni patches, D_{void}, are c1) 2.5 µm, c2) 5 µm, c3) 10 µm, and c4) 15 µm. Three circular Ni patches are placed on z = 0 µm as indicated by the gray blocks. The data are obtained from the cutlines at a height of 4 µm above Ni patches that is schematized in Figure S7 (Supporting Information). The gray dashed line indicates the minimal value (10^{12} A^2 m^{-3}) needed for trapping the SPC. d) The percentage of untrapped SPCs (D_{SPC} = 4.54 µm) under the conditions of various D_{patch} and D_{void} combinations.

in which ρ_p and ρ_l represent the densities of the SPC and the surrounding liquid, respectively, ζ represents the Gaussian random number and ranges from 0 to 1, m_p is the mass of the SPC, k_b is the Boltzmann constant, and η_f is the kinematic viscosity of the fluid surrounding the SPC. The Cunningham correction factor, C_{Cun}, accounts for the non-continuum effects of the drag force. As the Reynolds number, Re, is much smaller than unity in this study, the drag force is best described by Stokes' law. Here, the magnitude of the Brownian force (F_r) results from a dimensionless scaling analysis.[45]

In Figure 2c, effective gravitational force, $F_g - F_b$, and Brownian force F_r are calculated and compared to F_m. The dominating force is identified in a parameter space of patch and colloid size. The region Brownian force is dominant in the parameter range where $F_r/F_m > 1 \cap F_r/(F_g - F_b) > 1$ highlighted in white (F_r dominates). In this part of the parameter space, the SPC will not be easily trapped as the Brownian force dominates and randomizes the SPC motion counteracting trapping. The dark gray section of the parameter space (F_g dominates) corresponds to a region where gravitational force dominates ($(F_g - F_b)/F_m > 1 \cap (F_g - F_b)/F_r > 1$); hence, the SPC will sediment on the patch under the gravitational pull. The light gray region (F_m dominates) illustrates the parameter space where $F_m/F_r > 1 \cap F_m/(F_g - F_b) > 1$. In this region, F_m is larger than both the Brownian force and the gravitational force; therefore, the SPCs are expected to get trapped by the patch. This parameter phase diagram provides an overview in which forces dominate in the parameter space spanning D_{patch} and D_{void}. We found out that small Ni patches ($D_{patch} \leq \approx 0.67$ µm) only induce weak F_m, and therefore lead to the fact that the gravitational force $F_g - F_b$ dominates when $D_{SPC} \geq 2.2\,\mu\text{m}$. When the SPC is smaller than 2.2 µm the Brownian force, F_r, will dominate and complicate trapping. When $D_{patch} \geq \approx 4\,\mu\text{m}$, the magnetic force will always prevail regardless of the size of SPC.

We found that the size of the Ni patch influences the maximal height above the surface that magnetic forces reach while the shape of the patch remains insignificant. Figure S4 (Supporting Information) shows the sediment action speed for several practical D_{SPC} used in our experiments. The micrograients profiles of the magnetic field along the full x-z plane are numerically evaluated in Figure S3 (Supporting Information). From these profiles, we found that the diameter of the Ni patch determines the maximal elevation that the magnetic force can reach, and thus 'pull in' particles. Besides the patch size, various patch geometries are also numerically evaluated in Figures S5 and S6 (Supporting Information). These results emphasize that varying the patch geometry only has a minor effect on the resulting vertical magnetic force. For completeness, we show the SPC trajectory rebuilt using Particle tracking velocimetry in a microfluidic channel with various D_{patch} in Figure S10 (Supporting Information). These observations have a good agreement with the dominating force analysis.

2.2.2. Force Balance in Scenario B: Optimization the Magnetic Microgradient Along x Direction for Trapping Ratio

We proceed by considering a particle that happens to settle in the interstitial space between adjacent Ni patches. In this scenario, the SPC needs to move along *x*-axis to approach the Ni patches to get trapped, as illustrated in Figure 3b. Consequently, we focus on the horizontal *x* microgradient of the magnetic field and consider the horizontal component of the magnetic force.

$$F_{m,x} = 4\pi r^3 \mu_0 \frac{\chi_{part} - \chi_{sol}}{\chi_{part} + 2\chi_{sol} + 3} |\vec{H}| \frac{\partial |\vec{H}|}{\partial (x)} \tag{3}$$

To built a working understanding of the forces involved in scenario B, we investigate numerically how the distance between patches, D_{void}, influences magnetic microgradients for a fixed patch diameter D_{patch} in COMSOL. For the finite element calculations, three Ni patches are arranged with different "patch to void" ratios, i.e., D_{void}: D_{patch} = 0.5, 1, 2 and 3, respectively, whereas D_{patch} is canonically fixed as 5 µm. Here, we choose cutline at 4 µm high above the Ni patches (depicted in Figure S7, Supporting Information) to elaborate the horizontal microgradient because 4 µm is able to compensate the thickness of Polydimethylsiloxane (PDMS) layer (≈1 µm) and the size of SPC. The results are shown in Figure 3c. The minimal horizontal microgradient value is chosen as 10^{12} A^2 m^{-3}, corresponding to an effective force that makes that trapping occurs within experimentally reachable time spans. This cut-off value is plotted as a gray- dashed line. A more detailed contour plot for the microgradients in the xz-plane can be found in Figure S8 (Supporting Information).

As seen from Figure 3 c1,c2, for small D_{void}: D_{patch} value, i.e., 0.5 and 1 exhibit similar "seagull" profiles. The microgradient reaches its maximum value at the edge of the patches and gently descends as leaving the edge. The microgradient value is always above the minimum value of 10^{12} A^2 m^{-3}. Consequently, the SPCs will move toward the patches and will be trapped. Interestingly, the D_{void}: D_{patch} = 0.5 array induces smaller microgradient in the patch center as highlighted in green. It appears that the closely packed virtual moulds act as a single virtual mould because the magnetic dipoles cancel each other out in the center and yield a lower microgradient.[46] This observation is further clarified in Figure S9 (Supporting Information).

While small D_{void}: D_{patch} is not so ideal, larger ratios are not desirable at all. In Figure 3c3,c4 corresponding to D_{void}: D_{patch} = 2 and 3, the horizontal microgradients exhibit "cliff" profiles. The microgradient still reaches its maximum value at the patch edge but it precipitously goes below 10^{11} A^2 m^{-3} when moving to the interstitial spacing. As it falls below the gray line, a "dead zone" as indicated by the green shadow shows up. In Figure 3c4, the distance of this "dead zone" Δx is ≈5.8 µm. When Δx is larger than the SPC itself, a failure of trapping and consequently a higher untrapped ratio is foreseen. Note that in Figure 3c, the value of the valleys is supposed to be zero, which is smoothed by the mesh size and the steep gradient around it. Despite that, we consider the results reasonable because the forced objects are full spheres instead of point objects in reality.

To check the validity of trends observed in finite element calculations, a set of trapping experiments were run and the ratios of untrapped beads relative to total SPCs injected under two different D_{patch} with various D_{void} is presented in Figure 3d. For these analyses, the number of untrapped SPCs and the total number of SPCs injected were followed and counted with the

OpenCV package in Python. It can be seen that the percentage of untrapped beads increases from 0% to 9% for an increasing D_{void}, while the D_{patch} is set constant at 5 µm. A similar increase occurs from 1% to 7% for D_{patch} = 10 µm for an increasing D_{void} size. These experimental results are in good agreement with the numerical analysis.

2.2.3. Washing of the Untrapped Sedimented SPCs

From the discussions above, it is concluded that there is a delicate balance among the SPC size, patch size, patch distance, and microchannel height that has to be considered in order to achieve SPC assembly over the VMMs within a reasonable time. However, a large patch distance is always necessary in order to realize a position in the binary code that is not filled with a particle. This unfortunately will break this delicate balance. Such a dilemma is demonstrated in **Figure** 4a1 using 2 sets of patch arrays that can be decoded into "TUD" (Technical University of Delft) and "ETH" (Swiss Federal Institute of Technology). In these arrays, the patch represents for bit "1" and void for "0". Each row is composed of 8 bits and represents a letter. Unfortunately, only the letter "U" (01010101, see Figure 4b) possess the desirable arrangement, i.e., D_{void}: D_{patch} = 1, but the other letters are not ideally arranged. Consequently, we would foresee a high untrapped ratio with such an array according to the previous finite element analysis study.

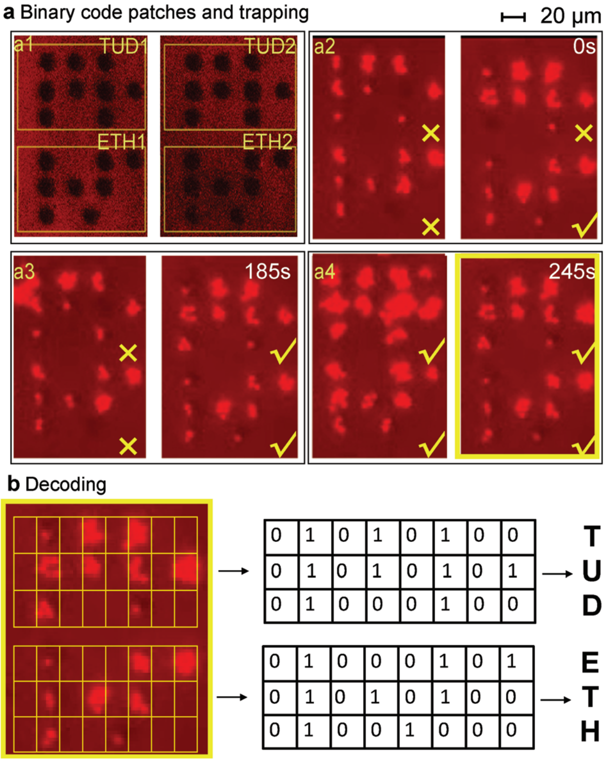

0	1	0	1	0	1	0	0	T
0	1	0	1	0	1	0	1	U
0	1	0	0	0	1	0	0	D

0	1	0	0	0	1	0	1	E
0	1	0	1	0	1	0	0	T
0	1	0	0	1	0	0	0	H

Figure 4. A demonstration of the wash strategy and decoding method. a) The Ni patches design that composed of binary-codes corresponding to abbreviation of institutes collaborating in this study "TUD" for Technical University of Delft and "ETH" for Swiss Federal Institute of Technology in Zürich. More effective binary codes were formed as the washing step went on. b) Illustration of the decoding process: the decoding method involves 3 steps. Step 1: read the barcode under microscope. Step 2: mesh the output image and identify the SPCs in each mesh, assign "1" to the matrix when SPC detected and " 0" otherwise. Step 3: translate the ASCII code into text.

To further improve our trapping efficiency, we incorporate a washing step into our protocol. To be more explicit, we use a polymer solution with no SPCs from a different inlet to wash away the untrapped SPCs over the voids while keeping the magnetic field on. This extra step takes place between the "Trap" step and the "Photo-polymerize" and is programmed as: pressure on, magnet on, and shutter closed. A demonstration of this step is shown in Movie S2 (Supporting Information) and a set of images extracted is illustrated in Figure 4a2–a4. When the washing step started, i.e., 0s in Figure 4a2, there was only one valid binary code as labeled by a checkmark. Along with the polymer solution flow, the untrapped SPCs were flushed through the channel and were trapped by the magnetic active patches that they passed by. In this way, the code efficiency increased from 25% at 0s (Figure 4a2) to 50% at 185 s (Figure 4a3), thus the fidelity of complex binary codes was improved. By increasing the washing time further, the number and the exact position of the SPCs may change from run to run but we can reproducibly incorporate the intended code to microparticles and decode the incorporated code. Finally, we have achieved 100% code efficiency at 245 s with an optimized initial SPC concentration (Figure 4a4).

In Figure 4b, we illustrate the optical decoding method: First, the microscope image of the binary code is captured as highlighted in yellow. The image is meshed to 3 by 8 individual code regions. Followed by that, the SPC in the individual area is identified and the value is attributed to a binary code. No matter how the morphology of the SPC aggregates in each mesh are, the code is read as "1" if there is any SPCs in this area or " 0" otherwise.

3. Conclusion

We present a microfluidic synthesis method for producing PEGDA microparticles with SPCs embedded at designated positions combining virtual magnetic moulds with stop–flow lithography. The hydrogel microparticles may function as an on-dose anti-counterfeiting measure for food and medicine. The embedded SPCs collectively act as a binary code matrix that can be read optically while their superparamagnetic nature makes the microparticles responsive to the magnetic field. However, we encountered undesired scenarios such as untrapped SPCs settling in interstitial gaps of our Ni patches, as well as excessive trapping times. These scenarios result in unreliable encoding and reading of the binary code as well as unacceptably long production times. To overcome these experimental challenges, a combined scaling argument and finite element study were conducted. We identified D_{void}: D_{patch} = 1 as the optimum experimental parameter to get a high trapping efficiency. Smaller or larger spacing will lead to a decline of magnetostatic force at the void and result in untrapped SPCs. To rule out such undesired scenarios, we proposed a washing strategy that has proven to compensate the undesired D_{void}: D_{patch} ratio in the binary code. The proposed magnetic microparticles may inspire the development of quality control, tracking, and anti-counterfeiting technologies in order to combat increasing counterfeiting crime. Besides that, this approach successfully assembles SPCs into anisotropic patterns and traps them in a hydrogel matrix with desired 3D geometry, showing potential for synthesis of magnetically responsive structures such as microswimmers, micro self-propeller and soft microrobots.

4. Experimental Section

Materials: Poly(ethylene glycol) diacrylate (average Mn 700), 2-Hydroxy-2-methylpropiophenone (CAS No. 7473-98-5), and grids for transmission electron microscopy (grid size 400 mesh × 62 μm pitch, nickel) were purchased from Sigma–Aldrich. Cinnamon Cassia oil (CAS No. 8007-80-5) was purchased from Aromaolie Ki-Line VOF. Sigma–Aldrich SYLGARD 184 silicone elastomer kit was purchased from Dow Corning. All the SPCs (S2451, S2180, AR488 and S246) with saturation magnetization values in the range from 15–25 $\mathrm{Am^2\ kg^{-1}}$ were purchased from MicroParticles GmbH, the densities of the colloids are 1.79, 1.62, 1.49, and 1.51 g $\mathrm{cm^{-3}}$ while the diameters are 1.43, 3.90, 4.54, and 10.3 μm, respectively. The SPC consists of a core made of polystyrene with iron oxide particles incorporated inside the polystyrene. The core is covered by a carboxyl group polymer shell with a thickness of 100–500 nm to prevent any leakage of the iron oxide particles to the surrounding medium. For easier observation, fluorescent dyes were also functionalized in the shell. The shell thickness is ignored in the calculations and simulations.

Fabrication of Magnetic Moulds: Nickel patches are deposited on a thin glass slide via e-beam deposition of nickel on a lithographically patterned surface. The protocol was similar to the literature,[19] followed by standard photolithography; after dissolving the exposed photoresist regions, a thin nickel layer was deposited by electron beam evaporation and the sacrificial layer was removed subsequently. The patterns of the Ni patches were controlled by the lithography mask. Despite that the ready patch was 200 nm thick due to the experimental constrain, it showed good magnetic interaction with the colloids.

Preparation of the Microfluidic Channel: Polydimethylsiloxane (PDMS) microfluidic devices were fabricated in a similar way as described in the literature.[7] A single straight channel design that is 35 μm in height, 1 cm in lengthm and 500 μm in width was used as since no complicated fluid was involved. After puncturing one 0.3 mm hole on each end of the channel using biopsy needle, the devices were attached to the magnetic patches slide with a thin layer of spin-coated and semicured (65 °C, 30 min, ratio base: curing agent = 10:1 wt.%) PDMS layer. The whole device was then cured at 65 °C overnight. The ready device was ≈2 mm in thickness and 10 mm by 10 mm in width and length.

Injected Suspension: The injected suspension is a mixture of photo-initiator (2-hydroxy-2-methylpropiophenone) with PEGDA-700 at a proportion 1:20 vol.% and without any magnetic content tuned to assure the edibility. To get a homogeneous distribution of the SPCs, the suspension was vortexed and placed in a sonication bath for 30 min at room temperature.

Microparticle Synthesis: The SFL setup was modified from the literature.[7] As depicted in Figure 1a, the microfluidic device was set with the Ni patch at the bottom and placed on a microscope (Nikon Ti-E inverted) that was equipped with a motorized stage. The inlet was connected to the remotely controlled air pump (0.5 psi) and the outlet to the collecting Eppendorf tube via silicone tubes. Andor CCD camera was hooked to the microscope to record the real-time tracking of the magnetic colloids' behavior. The external magnetic field was provided by an axially magnetized permanent neodymium magnet (TERRAMAG H-N 40/150 Permanent magnet Ring NdFeB) with a residual magnetism of 1.26 T. The ring shape made sure that it can be placed around the objective under the channel.

Finite Element Simulations: In COMSOL setting up, No Currents (mfnc) module was used alongside the finite elements method. The Ni patches ($\mu_r = 600$) were placed inside an air sphere ($\mu_r = 1$) that was four times larger than the Ni patches in diameter. Outside the air sphere, there was a second air shell in 5 μm thickness, which was defined as the layer for the finite element method. The homogeneous external magnetic field (H = 100 $\mathrm{KAm^{-1}}$ = 0.1245*T*) was set perpendicular to the Ni patches. A zero magnetic scalar potential (ΔV_m) was set at the bottom below the Ni patches. The constitutive relation applied is shown in Equation (4), and the reduced H-field is expressed as Equation (5) where H_b is the background magnetic field.

$$\nabla \vec{B} = \nabla(\mu_0 \mu_r \vec{H}) = 0 \tag{4}$$

$$\vec{H} = -\nabla V_m + \vec{H}_b \tag{5}$$

The microgradient $|\vec{H}|\frac{\partial|\vec{H}|}{\partial z}$ induced by Ni patches of different geometries, sizes, and arrangements were investigated in COMSOL. Lines and slices were cut along *z*-axis when assess the scenario in Figure 2b while *x*-axis for Figure 2c. ImageJ was applied where a measurement of the effective magnetostatic force height is needed.

It was assumed that the microchannel would be ≈20 μm, and most of the colloids would flow through the middle of the microchannel due to Hagen-Poiseuille flow. As such, the value of the $|\vec{H}|\frac{\partial|\vec{H}|}{\partial z}$ in the numerical study was all obtained from the cutlines at a height of 10 μm above the Ni patch (as schematically shown in Figure S7, Supporting Information) unless otherwise stated.

Supporting Information

Supporting Information is available from the Wiley Online Library or from the author.

Acknowledgements

This work is part of the research program open technology scheme with project number P80384, which is financed by the Dutch Research Council (NWO). A.F.D. was supported by the Swiss National Science Foundation through the National Centre of Competence in Research Bio-Inspired Materials (Grant No. 51NF40_182881).

Conflict of Interest

The authors declare no conflict of interest.

Data Availability Statement

The data that support the findings of this study are available in the supplementary material of this article.

Keywords

anti-counterfeiting, hydrogel microparticles, on-dose authentication

Received: April 22, 2022
Revised: July 22, 2022
Published online: September 4, 2022

---

[1] WHO, A study on the public health and socioeconomic impact of substandard and falsified medical products, report WHO/EMP/RHT/2017.02, World Health Organization **2017**.

[2] S. M. Beargie, C. R. Higgins, D. R. Evans, S. K. Laing, D. Erim, S. Ozawa, *PloS One* **2019**, *14*, e0217910.
[3] R. Shah, P. Prajapati, Y. Agrawal, *J. Adv. Pharm. Technol. Res.* **2010**, *1*, 368.
[4] M. Puddu, D. Paunescu, W. J. Stark, R. N. Grass, *ACS Nano* **2014**, *8*, 2677.
[5] H. Zhang, D. Hua, C. Huang, S. K. Samal, R. Xiong, F. Sauvage, K. Braeckmans, K. Remaut, S. C. De Smedt, *Adv. Mater.* **2020**, *32*, 1905486.
[6] H. B. Eral, E. R. Safai, B. Keshavarz, J. J. Kim, J. Lee, P. Doyle, *Langmuir* **2016**, *32*, 7198.
[7] I. Rehor, S. van Vreeswijk, T. Vermonden, W. E. Hennink, W. K. Kegel, H. B. Eral, *Small* **2017**, *13*, 1701804.
[8] Y. N. Vakkipurath Kodakkadan, K. Idzakovicova, J. Sepitka, D. ten Napel, E. Safai, P. Cigler, F. Štěpánek, I. Rehor, *Biomater. Sci.* **2020**, *8*, 3044.
[9] C. C. Schuurmans, A. Abbadessa, M. A. Bengtson, G. Pletikapic, H. B. Eral, G. Koenderink, R. Masereeuw, W. E. Hennink, T. Vermonden, *Soft Matter* **2018**, *14*, 6327.
[10] S. Han, H. J. Bae, J. Kim, S. Shin, S.-E. Choi, S. H. Lee, S. Kwon, W. Park, *Adv. Mater.* **2012**, *24*, 5924.
[11] Y. C. Saraswat, F. Ibis, L. Rossi, L. Sasso, H. B. Eral, P. Fanzio, *J. Colloid Interface Sci.* **2020**, *564*, 43.
[12] G. Tang, L. Chen, Z. Wang, S. Gao, Q. Qu, R. Xiong, K. Braeckmans, S. C. De Smedt, Y. S. Zhang, C. Huang, *Small* **2020**, *16*, 1907586.
[13] G. Tang, R. Xiong, D. Lv, R. X. Xu, K. Braeckmans, C. Huang, S. C. De Smedt, *Adv. Sci.* **2019**, *6*, 1802342.
[14] J. W. Leem, M. S. Kim, S. H. Choi, S.-R. Kim, S.-W. Kim, Y. M. Song, R. J. Young, Y. L. Kim, *Nat. Commun.* **2020**, *11*, 328.
[15] S. J. Trenfield, H. Xian Tan, A. Awad, A. Buanz, S. Gaisford, A. W. Basit, A. Goyanes, *Int. J. Pharm.* **2019**, *567*, 118443.
[16] Z. Grof, F. Štěpánek, *Comput. Chem. Eng.* **2021**, *154*, 107492.
[17] S. Takei, *Appl. Phys. Express* **2018**, *11*, 8.
[18] D. Dendukuri, S. S. Gu, D. C. Pregibon, T. A. Hatton, P. S. Doyle, *Lab Chip* **2007**, *7*, 818.
[19] A. F. Demirörs, P. P. Pillai, B. Kowalczyk, B. A. Grzybowski, *Nature* **2013**, *503*, 99.
[20] R. N. Georgiev, S. O. Toscano, W. E. Uspal, B. Bet, S. Samin, R. van Roij, H. B. Eral, *Proc. Natl. Acad. Sci. USA* **2020**, *117*, 21865.
[21] H. Z. An, E. R. Safai, H. B. Eral, P. S. Doyle, *Lab Chip* **2013**, *13*, 4765.
[22] D. Dendukuri, D. C. Pregibon, J. Collins, T. A. Hatton, P. S. Doyle, *Nat. Mater.* **2006**, *5*, 365.
[23] H. Z. An, H. B. Eral, L. Chen, M. B. Chen, P. S. Doyle, *Soft Matter* **2014**, *10*, 7595.
[24] D. C. Pregibon, M. Toner, P. S. Doyle, *Langmuir* **2006**, *22*, 5122.
[25] J. Lee, P. W. Bisso, R. L. Srinivas, J. J. Kim, A. J. Swiston, P. S. Doyle, *Nat. Mater.* **2014**, *13*, 524.
[26] Y. Dou, B. Wang, M. Jin, Y. Yu, G. Zhou, L. Shui, *J. Micromech. Microeng.* **2017**, *27*, 113002.
[27] R. A. Hughes, E. Menumerov, S. Neretina, *Nanotechnology* **2017**, *28*, 282002.
[28] L. Wang, S. Dong, J. Hao, *Curr. Opin. Colloid Interface Sci.* **2018**, *35*, 81.
[29] Y. N. V. Kodakkadan, K. Idzakovicova, J. Sepitka, D. Ten Napel, E. Safai, P. Cigler, F. Štěpánek, I. Rehor, *Biomater. Sci.* **2020**, *8*, 3044.
[30] I. Rehor, C. Maslen, P. G. Moerman, B. G. Van Ravensteijn, R. Van Alst, J. Groenewold, H. B. Eral, W. K. Kegel, *Soft Rob.* **2021**, *8*, 10.
[31] M. E. Helgeson, S. C. Chapin, P. S. Doyle, *Curr. Opin. Colloid Interface Sci.* **2011**, *16*, 106.
[32] A. Kjar, Y. Huang, *Pharmaceutics* **2019**, *11*, 390.
[33] J. Fei, R. Liu, *Mater. Sci. Eng., C* **2016**, *63*, 657.
[34] Y. C. Saraswat, F. Ibis, L. Rossi, L. Sasso, H. B. Eral, P. Fanzio, *J. Colloid Interface Sci.* **2020**, *564*, 43.
[35] P. Xue, X. Zhang, Y. J. Chuah, Y. Wu, Y. Kang, *RSC Adv.* **2015**, *5*, 75204.
[36] D.-E. Coricovac, E.-A. Moacă, I. Pinzaru, C. Cîtu, C. Soica, C.-V. Mihali, C. Păcurariu, V. A. Tutelyan, A. Tsatsakis, C.-A. Dehelean, *Frontiers in Pharmacology* **2017**, *8*, 154.
[37] P. Panda, S. Ali, E. Lo, B. G. Chung, T. A. Hatton, A. Khademhosseini, P. S. Doyle, *Lab Chip* **2008**, *8*, 1056.
[38] A. Sun, X. He, X. Ji, D. Hu, M. Pan, L. Zhang, Z. Qian, *Chin. Chem. Lett.* **2021**, *32*, 2117.
[39] H. B. Eral, E. R. Safai, B. Keshavarz, J. J. Kim, J. Lee, P. S. Doyle, *Langmuir* **2016**, *32*, 7198.
[40] C. C. L. Schuurmans, A. Abbadessa, M. A. Bengtson, G. Pletikapic, H. B. Eral, G. Koenderink, R. Masereeuw, W. E. Hennink, T. Vermonden, *Soft Matter* **2018**, *14*, 6327.
[41] H. Z. An, H. B. Eral, L. Chen, M. B. Chen, P. S. Doyle, *Soft Matter* **2014**, *10*, 7595.
[42] A. Cavallo, M. Madaghiele, U. Masullo, M. G. Lionetto, A. Sannino, *J. Appl. Polym. Sci.* **2017**, *134*, 2.
[43] Z. Lou, W. Wang, C. Yuan, Y. Zhang, Y. Li, L. Yang, *Journal of Bioresources and Bioproducts* **2019**, *4*, 43.
[44] G.-H. Chen, H.-S. Chen, *ACS Appl. Nano Mater.* **2020**, *3*, 8858.
[45] A. Li, G. Ahmadi, *Aerosol Sci. Technol.* **1992**, *16*, 209.
[46] D. N. Boon, Thesis consultant, Asvalt AB., Accessed: 04-2019 untill 03-2020.